LETTER

doi:10.1038/nature20146

Greenland was nearly ice-free for extended periods during the Pleistocene

Joerg M. Schaefer[1,2], Robert C. Finkel[1,3], Greg Balco[4], Richard B. Alley[5], Marc W. Caffee[6], Jason P. Briner[7], Nicolas E. Young[1], Anthony J. Gow[8] & Roseanne Schwartz[1]

The Greenland Ice Sheet (GIS) contains the equivalent of 7.4 metres of global sea-level rise[1]. Its stability in our warming climate is therefore a pressing concern. However, the sparse proxy evidence of the palaeo-stability of the GIS means that its history is controversial (compare refs 2 and 3 to ref. 4). Here we show that Greenland was deglaciated for extended periods during the Pleistocene epoch (from 2.6 million years ago to 11,700 years ago), based on new measurements of cosmic-ray-produced beryllium and aluminium isotopes (^{10}Be and ^{26}Al) in a bedrock core from beneath an ice core near the GIS summit. Models indicate that when this bedrock site is ice-free, any remaining ice is concentrated in the eastern Greenland highlands and the GIS is reduced to less than ten per cent of its current volume. Our results narrow the spectrum of possible GIS histories: the longest period of stability of the present ice sheet that is consistent with the measurements is 1.1 million years, assuming that this was preceded by more than 280,000 years of ice-free conditions. Other scenarios, in which Greenland was ice-free during any or all Pleistocene interglacials, may be more realistic. Our observations are incompatible with most existing model simulations that present a continuously existing Pleistocene GIS. Future simulations of the GIS should take into account that Greenland was nearly ice-free for extended periods under Pleistocene climate forcing.

The possibility that future warming will cause destabilization of the GIS has motivated the use of geological records to estimate the climate sensitivity of the GIS. Terrestrial studies[2,3] have argued that the palaeo-environment of the Kap Kobenhavn Formation in north Greenland implied an ice-free Greenland, with temperatures nearly 6 °C above present persisting for about 20,000 years (20 kyr) from 1.8 million years (Myr) ago to 2.0 Myr ago. Marine sedimentary proxy data from sites off southwest Greenland[5,6] are interpreted to indicate a smaller GIS during both the Marine Isotope Stage (MIS) 5e (or Eemian; about 120 kyr ago) and MIS 11 (about 410 kyr ago) interglacial periods. Biomolecules in basal ice of the Dye-3 ice core in southern Greenland provide evidence for subarctic conditions (and thus a smaller GIS) sometime in the past million years or so[7] and a recent review[8] argues that the near-field and far-field data require major ice-sheet fluctuations, and allow (but do not require) near-total ice loss during the Pleistocene. On the other hand, data from the basal NEEM ice core[9] indicate minor ice-surface lowering during MIS 5e despite temperatures several degrees warmer than present. The geochemistry of Greenland Ice Sheet Project Two (GISP2) silty basal ice has been interpreted as being consistent with the scenario of continuous ice cover for the past 2.6 Myr (ref. 4) and trapped air enclosed in the silty ice layer of the nearby Greenland Ice Sheet Project (GISP) core indicate basal ice ages exceeding 1 Myr (ref. 10; Methods).

The GIS survived mid-Holocene temperatures somewhat warmer than those of the past millennium and many model simulations show a relatively stable GIS over the interglacials of the recent geologic past[11,12]. However, simulations also show that the warming required to remove most of the GIS is model-dependent and sensitive to external forcings and internal feedbacks, including insolation forcing, accumulation rate parameterization, and distribution and seasonality of temperature. Results imply temperature thresholds for ice-sheet stability between one[11] and a few degrees Celsius above present temperatures (see review in ref. 8; also refs 13 and 14). Because the GIS sensitivity probably changes with increasing forcing temperature, model timescales for ice-sheet removal depend on the amplitude of the forcing: a temperature threshold of 2 °C with a 5,000-year response time given 3 °C warming was inferred by ref. 13, but more extreme temperature forcing allows for GIS removal within a few thousand or even several hundred years[13]. Thus, current model results remain ambiguous but do show that both the magnitude and the duration of warmth are important to ice-sheet deglaciation.

Overall, existing geological data and model experiments have not resolved the question of whether the GIS disappeared or shrank substantially in warm interglacial periods. Much of this uncertainty reflects the fact that the geological data mostly comprise inference from remote proxy records, since direct evidence, if it exists, is buried beneath the present ice sheet. Here we attempt to overcome this obstacle via cosmogenic nuclide analysis of sub-GIS bedrock.

On 1 July 1993, after five years of drilling and recovery of a 3,040.3-m-long ice core and a 13.1-m-long core of sediment-rich basal ice, the GISP2 project penetrated 1.55 m of bedrock[15] (Figs 1 and 2). We describe measurements of cosmic-ray-produced in-situ ^{10}Be and ^{26}Al from this GISP2 bedrock core. ^{10}Be and ^{26}Al, with half-lives of 1.4 Myr (refs 16 and 17) and 0.7 Myr (ref. 18) respectively, are trace radionuclides produced in situ by nuclear interactions between cosmic-ray particles and rocks exposed at Earth's surface. The cosmic-ray flux decreases exponentially with an e-folding length ($1/e \approx 0.37$) of about 60 cm in rock or about 1.5 m in ice, so cosmogenic-nuclide production is negligible beneath ice sheets. The presence of any substantial *in situ* cosmogenic radionuclide concentration in subglacial bedrock indicates geologically recent near-surface exposure and thus ice-free conditions. Pioneering analysis in the 1990s, published as an abstract[19], indicated detectable ^{10}Be and ^{26}Al in the GISP2 bedrock core, but overall uncertainties remained large enough to prevent unambiguous conclusions about past GIS change. Here we describe comprehensive new ^{10}Be and ^{26}Al measurements, a detailed analysis of the data, and their implications for past GIS dynamics.

After separating and purifying quartz from segments of bedrock core (Methods), we combined aliquots into the largest number of depth

[1]Lamont-Doherty Earth Observatory, Geochemistry, Palisades, New York 10964, USA. [2]Department of Earth and Environmental Sciences, Columbia University, New York, New York 10027, USA. [3]Department of Earth and Planetary Sciences, University of California, Berkeley, Berkeley, California 95064, USA. [4]Berkeley Geochronology Center, 2455 Ridge Road, Berkeley, California 94709, USA. [5]Department of Geosciences, Pennsylvania State University, University Park, PA 16802, USA. [6]Department of Physics and Astronomy, Purdue University, 525 Northwestern Avenue, West Lafayette, Indiana 47907, USA. [7]Department of Geology, University at Buffalo, Buffalo, New York 14260, USA. [8]US Army Cold Regions Research and Engineering Laboratory, Hanover, New Hampshire 03755, USA.

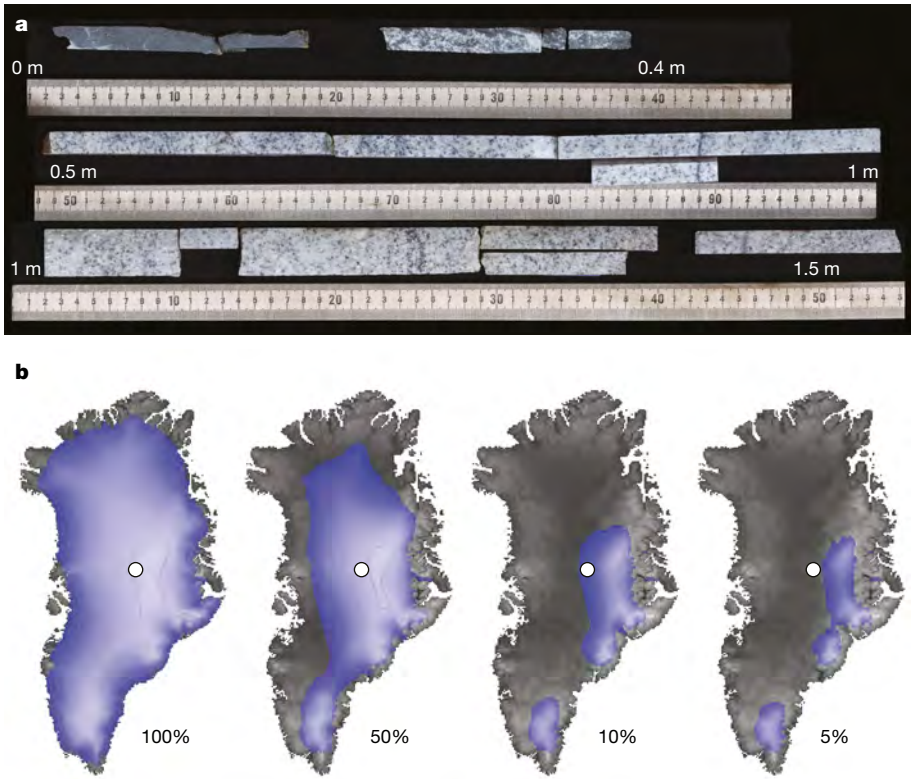

Figure 1 | The GISP2 bedrock core and GIS deglaciation. a, The GISP2 bedrock core. Note the lithologic transition from the top piece (carbonate) to granitoid and the excellent condition of the core (photo copyright Geoffrey Hargreaves, National Ice Core Laboratory, Denver, 2015). **b**, Snapshots of GIS deglaciation ranging from 100% to 5% ice volume relative to today, from simulations by the Penn State University Ice Sheet Model (PSU) coupled to the Victoria Earth System Model (UVic ESCM). The white circle indicates the GISP2 site. Similar model simulations, such as given in ref. 26, reveal this as a robust spatial deglaciation pattern of the GIS and show that when the GISP2 site is ice-free, only small ice remnants in the east Greenland highlands exist. Image adapted from ref. 27, Springer-Verlag.

increments consistent with maintaining the minimum sample size needed for accurate measurements (Fig. 1). This yielded in situ ^{10}Be measurements for five distinct segments (Fig. 2). For ^{26}Al, we further combined samples to make two amalgamated samples for precise ^{26}Al/^{27}Al measurements (GISP2/3 combined with GISP4 and GISP5/6 combined with GISP7; see Fig. 2, Methods and Extended Data Tables 1–3).

^{10}Be concentrations range from 9,800 ± 490 atoms g^{-1} to 24,800 ± 740 atoms g^{-1} and ^{26}Al concentrations are 54,900 ± 5,400 atoms g^{-1} to 88,000 ± 5,200 atoms g^{-1} (Fig. 2; Extended Data Tables 2 and 3; errors reported here and elsewhere are 1σ). These are one to two orders of magnitude above blank levels and three to four orders of magnitude above the concentration expected from cosmogenic-nuclide production by deeply penetrating cosmic-ray muons at the base of a 3-km-thick ice sheet[20,21] (Methods).

The measured in situ ^{26}Al/^{10}Be ratios are 4.2 ± 0.3 in the top sample and 4.1 ± 0.6 in the lower sample (Extended Data Table 1), significantly below the surface production ratio[22] of 6.75. This indicates that the period of surface exposure recorded by ^{10}Be and ^{26}Al concentrations was followed by a considerable period of time during which samples were deeply enough buried, presumably by the GIS, to stop the cosmic-ray flux (for example, see ref. 23) and let the ^{26}Al/^{10}Be ratio 'decay' during burial, with an apparent half-life of 1.4 Myr (Methods). These ^{26}Al/^{10}Be ratios limit the duration of continuous ice cover of the GISP2 bedrock to a maximum duration of 1.1 ± 0.1 Myr.

The measured in situ ^{10}Be and ^{26}Al concentrations themselves and their variation with depth mean that the GISP2 site must have been ice-free for a considerable period of time in the recent geologic past. The approximate e-folding length of the measured ^{10}Be concentration depth profile is nearly 260 g cm^{-2} (Methods), which requires contributions both from high-energy neutron spallation (predominant at the surface, decreasing with an e-folding length near 140 g cm^{-2}) and muon interactions (dominant below a depth of a few metres, with an e-folding length exceeding 1,500 g cm^{-1}) (refs 2 and 24). This both shows that samples were close to the surface when exposed to the cosmic-ray flux, and allows us to estimate their depth below the surface at that time (Methods). The data are best explained by 350 ± 20 g cm^{-2} of cover above the present bedrock surface, that is, about 1.3 m of rock, about 2 m of soil, or about 4 m of ice (Fig. 2; Methods). Thus, not even a thin ice cap could have been present at this site during the period of exposure. In addition, our data limit possible subglacial erosion at the GISP2 site to no more than 1–2 m during the period the site has been covered by the ice sheet, consistent with long-term[4] and modern observations[25] (Methods). Given this thickness of cover of the bedrock surface during exposure, the shortest exposure period consistent with the measurements is 280 ± 30 kyr (Methods).

Simulations of Greenland deglaciation in warm climates consistently predict the GISP2 site to be one of the last parts of the ice sheet to disappear; when it is ice-free, only a small ice cap in the eastern highlands remains[26,27] (Fig. 1; Methods), preserving old ice[10]. This implies that when GISP2 bedrock was exposed to the surface cosmic-ray flux, more than 90% of the entire GIS was absent.

Although we cannot identify a unique ice-cover history, the ^{10}Be and ^{26}Al data can be used to test specific Pleistocene GIS change scenarios that are or are not consistent with the data (Fig. 3). The simplest scenario consistent with the data, which also provides an upper limit on the length of time the present GIS has been stable, consists of more than 280 ± 30 kyr of ice-free conditions followed by 1.1 ± 0.1 Myr of continuous ice cover (the maximum-stability scenario '1' in Fig. 3; see Methods). If the ice sheet had been continuously present for longer, the ^{26}Al/^{10}Be ratios would be lower than observed (for example, continuous ice cover over the past 2.6 Myr implies an ^{26}Al/^{10}Be ratio no higher than 2).

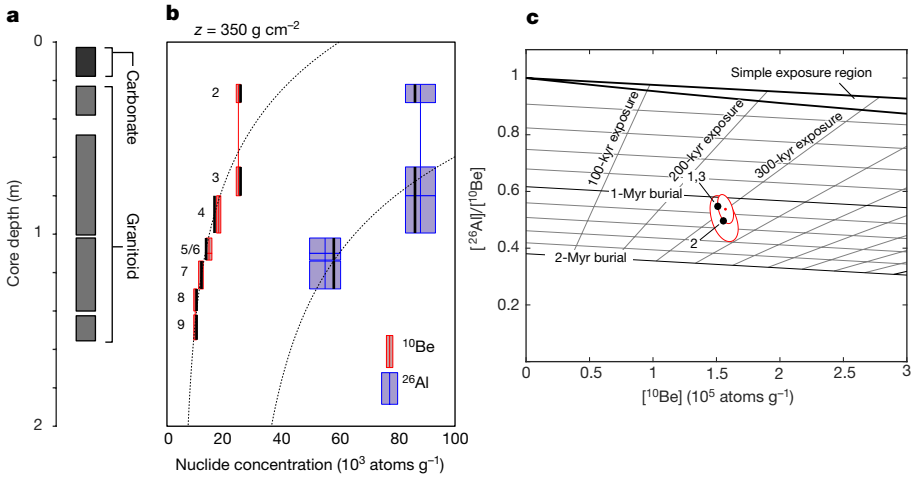

Figure 2 | ^{10}Be and ^{26}Al data for the GISP2 bedrock. a, Schematic core stratigraphy showing core recovery. Image adapted from ref. 15, International Glaciological Society. **b**, ^{10}Be and ^{26}Al concentrations in core segments, numbered in black. Heights of boxes correspond to the length of core segments. Thin vertical lines connect stacked samples that we amalgamated for single measurement where necessary. Specifically, for ^{10}Be measurements, we combined the individual core segments as follows: (1) GISP2 and GISP3; (2) GISP4; (3) GISP5 and GISP6; (4) GISP7; (5) GISP8 and GISP9; for ^{26}Al we combined GISP2, GISP3 and GISP4 for the analysis of the top sample and GISP5, GISP6 and GISP7 for the lower sample; please note that GISP5 and GISP6, and GISP8 and GISP9 are difficult to detect in the figure as individual samples. Widths of boxes show 1σ measurement uncertainties. Black dashed lines show predicted nuclide concentrations as a function of depth for the best-fitting bedrock cover thickness (350 g cm^{-2}) and the maximum-stability GIS exposure–burial scenario ('1' in Fig. 3). Heavy black lines are predicted nuclide concentrations averaged over depth ranges corresponding to each measurement; our fitting procedure (see Methods) minimizes the mismatch between these and the measurements. **c**, Two-nuclide diagram comparing measured ^{10}Be and ^{26}Al concentrations, normalized to production rates beneath 350 g cm^{-2} cover of the bedrock surface, with predicted concentrations for various exposure histories (see ref. 29 for a complete explanation of this kind of diagram). Red ellipses are 68% confidence intervals on the measurements, considering measurement uncertainty only. Grid shows isolines of exposure and burial time for idealized two-stage exposure histories. Black dots show predicted nuclide concentrations for exposure histories, numbered as in Fig. 3.

However, this maximum-stability scenario does not resemble available palaeoclimate data[28] (Fig. 3; Methods). Other, more complex GIS change scenarios are equally consistent with our observations, subject to the constraints that the most recent ice-free period ended no longer than 1.1 ± 0.1 Myr ago, and that the smaller the number of distinct ice-free periods, the longer the duration of each period must be. For example, an opposite endmember that implies minimal long-term GIS stability is an episodic steady-state scenario in which Greenland was ice-free for 8 kyr of each 100-kyr glacial–interglacial cycle spanning several million years (the minimum-stability scenario '2' in Fig. 3). More realistic intermediate scenarios in which Greenland was ice-free for several thousand years during numerous (but not all) major Pleistocene interglacials, including MIS 11 as hypothesized from marine proxy records[5,6], are also consistent with the measurements (the multiple-exposures scenario '3' in Fig. 3).

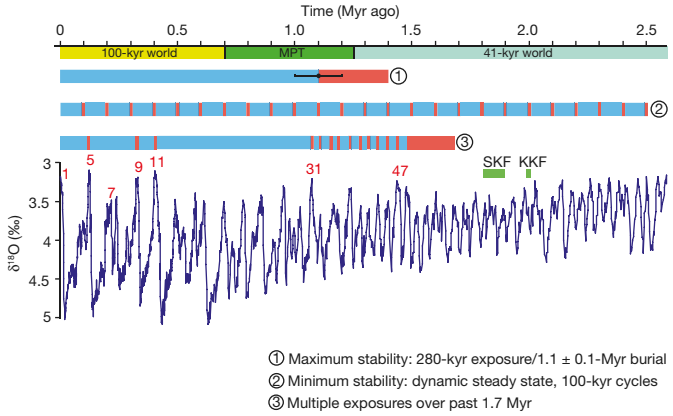

Figure 3 | Exposure–burial scenarios consistent with the data. Exemplary exposure–burial scenarios for the GISP2 bedrock core over the past 2.6 Myr that are consistent with the data, plotted over the climate record derived from stacked benthic foraminifera[30], a proxy for global ice volume and deep-ocean temperature. The horizontal bars show three such scenarios consistent with observations for the GISP2 bedrock site, including the maximum-stability GIS scenario '1', with red periods representing exposure of the GISP2 location and blue periods representing burial by the GIS overlying the GISP2 site. Small numbers in red above the climate curve indicate prominent interglacial marine isotope stages. The MPT (0.7–1.2 Myr ago) is the transition period from the early Pleistocene (41-kyr glacial–interglacial periodicity) to the mid-/late Pleistocene (100-kyr glacial–interglacial periodicity). The Store Koldewey Formation[2] (SKF) and the Kap Kobenhavn Formation[2,3] (KKF) are Quaternary sediment formations in northern Greenland, indicating that Greenland was nearly ice-free at that time.

Our observations preclude any scenario in which the GIS was continually present throughout the entire Pleistocene. The data require ice-free periods in Greenland during the interval of 41-kyr-long glacial–interglacial cycles and permit (but do not require) subsequent ice-free periods during the Mid-Pleistocene Transition (MPT) or the interval of 100-kyr-long glacial–interglacial cycles (Fig. 3).

To summarize, direct and robust evidence from the GISP2 bedrock core shows that the GIS was almost completely absent for an extended period of time during the Pleistocene. Our results do not directly determine the ice-dynamical processes responsible for the GIS deglaciation, but this first-order result is incompatible with many existing ice-sheet models or their respective climate-driving scenarios and provides important constraints for future simulations of past and future changes of the GIS. Models driven by boundary conditions appropriate to the warmest and most pronounced Pleistocene interglaciations must simulate the near-total disappearance of the ice sheet.

Online Content Methods, along with any additional Extended Data display items and Source Data, are available in the online version of the paper; references unique to these sections appear only in the online paper.

Received 12 June; accepted 5 October 2016.

1. Houghton, J. T. *et al.* (eds) *Climate Change 2001: The Scientific Basis. Contribution of Working Group I to the Third Assessment Report of the Intergovernmental Panel on Climate Change (IPCC)* (Cambridge Univ. Press, 2001).

2. Bennike, O. *et al.* Early Pleistocene sediments on Store Koldewey, northeast Greenland. *Boreas* **39,** 603–619 (2010).
3. Funder, S., Bennike, O., Bocher, J., Israelson, C. & Petersen, K. S. Late Pliocene Greenland—the Kap Kobenhavn Formation in North Greenland. *Bull. Geol. Soc. Den.* **48,** 117–134 (2001).
4. Bierman, P. R. *et al.* Preservation of a preglacial landscape under the center of the Greenland Ice Sheet. *Science* **344,** 402–405 (2014).
5. de Vernal, A. & Hillaire-Marcel, C. Natural variability of Greenland climate, vegetation, and ice volume during the past million years. *Science* **320,** 1622–1625 (2008).
6. Reyes, A. V. *et al.* South Greenland ice-sheet collapse during Marine Isotope Stage 11. *Nature* **510,** 525–528 (2014).
7. Willerslev, E. *et al.* Ancient biomolecules from deep ice cores reveal a forested Southern Greenland. *Science* **317,** 111–114 (2007).
8. Alley, R. B. *et al.* History of the Greenland Ice Sheet: paleoclimatic insights. *Quat. Sci. Rev.* **29,** 1728–1756 (2010).
9. NEEM Community Members. Eemian interglacial reconstructed from a Greenland folded ice core. *Nature* **493,** 489–494 (2013).
10. Yau, A. M., Bender, M. L., Blunier, T. & Jouzel, J. Setting a chronology for the basal ice at Dye-3 and GRIP: implications for the long-term stability of the Greenland Ice Sheet. *Earth Planet. Sci. Lett.* **451,** 1–9 (2016).
11. Calov, R., Robinson, A., Perrette, M. & Ganopolski, A. Simulating the Greenland ice sheet under present-day and palaeo constraints including a new discharge parameterization. *Cryosphere* **9,** 179–196 (2015).
12. Otto-Bliesner, B. L. & Brady, E. C. The sensitivity of the climate response to the magnitude and location of freshwater forcing: last glacial maximum experiments. *Quat. Sci. Rev.* **29,** 56–73 (2010).
13. Applegate, P. J., Parizek, B. R., Nicholas, R. E., Alley, R. B. & Keller, K. Increasing temperature forcing reduces the Greenland Ice Sheet's response time scale. *Clim. Dyn.* **45,** 2001–2011 (2015).
14. Stone, E. J., Lunt, D. J., Rutt, I. C. & Hanna, E. Investigating the sensitivity of numerical model simulations of the modern state of the Greenland ice-sheet and its future response to climate change. *Cryosphere* **4,** 397–417 (2010).
15. Gow, A. J. & Meese, D. A. Nature of basal debris in the GISP2 and Byrd ice cores and its relevance to bed processes. In *Proceedings of the International Symposium on Glacial Erosion and Sedimentation* (ed. Collins, D.) 134–140 (International Glaciological Society, 1996).
16. Chmeleff, J., von Blanckenburg, F., Kossert, K. & Jakob, D. Determination of the Be-10 half-life by multicollector ICP-MS and liquid scintillation counting. *Nucl. Instrum. Methods Phys. Res. B* **268,** 192–199 (2010).
17. Korschinek, G. *et al.* A new value for the half-life of Be-10 by heavy-ion elastic recoil detection and liquid scintillation counting. *Nucl. Instrum. Methods Phys. Res. B* **268,** 187–191 (2010).
18. Nishiizumi, K. *et al.* Absolute calibration of ^{10}Be AMS standards. *Nucl. Instrum. Methods Phys. Res. B* **258,** 403–413 (2007).
19. Nishiizumi, K. *et al.* In situ produced cosmogenic nuclides in GISP2 rock core from Greenland Summit. *Eos* **77,** F428, abstr. OS41B-10 (1996).
20. Heisinger, B. *et al.* Production of selected cosmogenic radionuclides by muons: 2. Capture of negative muons. *Earth Planet. Sci. Lett.* **200,** 357–369 (2002).
21. Heisinger, B. *et al.* Production of selected cosmogenic radionuclides by muons. 1. Fast muons. *Earth Planet. Sci. Lett.* **200,** 345–355 (2002).
22. Balco, G. & Rovey, C. W. An isochron method for cosmogenic-nuclide dating of buried soils and sediments. *Am. J. Sci.* **308,** 1083–1114 (2008).
23. Granger, D. E. & Muzikar, P. F. Dating sediment burial with in situ-produced cosmogenic nuclides: theory, techniques, and limitations. *Earth Planet. Sci. Lett.* **188,** 269–281 (2001).
24. Marrero, S. M. *et al.* Cosmogenic nuclide systematics and the CRONUScalc program. *Quat. Geochronol.* **31,** 160–187 (2016).
25. Bender, M. L., Burgess, E., Alley, R. B., Barnett, B. & Clow, G. D. On the nature of the dirty ice at the bottom of the GISP2 ice core. *Earth Planet. Sci. Lett.* **299,** 466–473 (2010).
26. Alley, R. B., Clark, P. U., Huybrechts, P. & Joughin, I. Ice-sheet and sea-level changes. *Science* **310,** 456–460 (2005).
27. Fyke, J., Eby, M., Mackintosh, A. & Weaver, A. Impact of climate sensitivity and polar amplification on projections of Greenland Ice Sheet loss. *Clim. Dyn.* **43,** 2249–2260 (2014).
28. Dutton, A. *et al.* Sea-level rise due to polar ice-sheet mass loss during past warm periods. *Science* **349,** (2015).
29. Granger, D. E. in *In-Situ Produced Cosmogenic Nuclides And Quantification Of Geological Processes* (eds Siame, L., Bourles, D. & Brown, E. T.) Spec. Pap. 415, 1–16 (The Geological Society of America, 2006).
30. Lisiecki, L. E. & Raymo, M. E. A Pliocene-Pleistocene stack of 57 globally distributed benthic delta O-18 records. *Paleoceanography* **20,** PA1003 (2005).

Acknowledgements We gratefully acknowledge help from the National Ice Core Laboratory (NICL) and thank the GISP2 steering committee for providing the bedrock core samples. J.M.S. acknowledges support by the Lamont Climate Center and the Comer Family Foundation. R.B.A. acknowledges support by the NSF (AGS 1338832), as do J.M.S., J.P.B. and N.E.Y. (PLR Arctic System Science Program number 1503959). We thank J. Fyke for assistance in producing Fig. 1b. G.B. acknowledges support from the Ann and Gordon Getty Foundation. M.W.C. acknowledges support from the US National Science Foundation, grant EAR-1153689. The pioneering cosmogenic-nuclide study of the GISP2 bedrock core under the lead of Kuni Nishiizumi in the late 1990s motivated our study. This is LDEO publication number 8068.

Author Contributions J.M.S. and R.C.F. initiated and coordinated the project, were in charge of the data production and wrote the first draft of the manuscript. G.B. provided the data analysis. R.B.A. participated in the GISP2 project, and provided glaciological expertise and model perspective. A.J.G. was part of the first scientist team at the GISP2 camp when the bedrock core was retrieved, examined the rock core and provided stratigraphic ice-bedrock expertise. M.W.C. measured the samples for Al isotopes. R.S. processed all the rock samples and did the Al and Be extraction. J.P.B. and N.E.Y. provided Arctic glacier expertise and prepared final figures. All authors read and edited multiple versions of the manuscript.

Author Information Reprints and permissions information is available at www.nature.com/reprints. The authors declare no competing financial interests. Readers are welcome to comment on the online version of the paper. Correspondence and requests for materials should be addressed to J.M.S. (schaefer@ldeo.columbia.edu).

Reviewer Information *Nature* thanks P.-H. Blard, G. Milne and the other anonymous reviewer(s) for their contribution to the peer review of this work.

METHODS

Analytical methods. We received either half- or quarter-splits of depth intervals from the 3.4-cm-diameter core (Fig. 1). After separating a quartz fraction from each core segment, in most cases we combined quartz fractions from multiple core segments to yield sufficient quartz for ^{10}Be and ^{26}Al analyses. Quartz separation, purification and Be and Al extraction from quartz then followed standard procedures used at the Lamont Cosmogenic Nuclide Laboratory[31]. After Be and Al extraction, we further combined Al fractions to obtain sufficient Al for ^{26}Al measurements. Thus, more core segments were combined for ^{26}Al analysis than for ^{10}Be, resulting in fewer ^{26}Al analyses overall (Fig. 2). Note that we are not including in further discussion a preliminary ^{26}Al measurement from the lowest core segments (GISP8 and GISP9), because we could not verify the Al yield in the extraction chemistry (Extended Data Table 3). In view of the importance of these specific samples and the possibility that the concentrations would be close to background levels, we added additional quality-control procedures. These include expanded monitoring of process blanks (Extended Data Tables 2 and 3), time-progressive blank corrections for the aluminium isotope measurements (see below) and ICP-OES standardization by in-house, gravimetrically prepared ^{27}Al standards cross-checked with commercial standards. Be and Al isotope ratio measurements by accelerator mass spectrometry (AMS) were carried out at the Center for Accelerator Mass Spectrometry at the Lawrence Livermore National Laboratory[32] and PRIME Laboratory, Purdue University, respectively.

^{26}Al/^{27}Al analysis at PRIME Laboratory. Until recently, most AMS measurements of the ^{26}Al/^{27}Al ratio used Al^- as the secondary ion. Injecting Al^- has the advantage that Mg^- is not formed, so ^{26}Mg, the main interference for ^{26}Al measurements, is not present. However, Al^- currents are low (typically 1 μA or less). Injecting AlO^- improves beam current by a factor of ten[33], thereby increasing the number of ^{26}Al counts measured at the detector. However, MgO^- is also produced, injected and accelerated, allowing ^{26}Mg to reach the detector. The gas-filled magnet installed at PRIME Laboratory allows effective suppression of this ^{26}Mg interference[34]. Specifically, N_2 at low pressure is bled into the beam line as it passes between the poles of a specially designed magnet placed before the traditional dE/dx detector[35]. ^{26}Mg and ^{26}Al ions have different charge-exchange cross-sections with N_2. Thus they have different charge states as they traverse the curved part of the flight tube passing through the magnet and therefore have different radii of curvature. An aperture at the magnet exit then suppresses ^{26}Mg ions by a factor of about 10^4 while allowing ^{26}Al into the detector. The ^{26}Al and some residual ^{26}Mg enter the detector. For low count rates (<1,000 counts per second), the dE/dx detector is able to distinguish these ions unambiguously on the basis of their energy-loss properties. The gas-filled magnet allows much greater secondary ion currents and allows the precision of ^{26}Al/^{27}Al measurements to approach that of ^{10}Be/^{9}Be measurements[36].

For ^{26}Al/^{27}Al measurement the tandem is run at a terminal voltage of 8.5 MV. Al ions in charge state +7 with an energy of around 65 MeV are selected. The ^{26}Al loses about a third of its energy traversing the gas-filled magnet, the remaining two-thirds being available for particle identification in the dE/dx detector. The samples analysed for this work had uniformly low Mg count rates, so the ^{26}Al particle peak was well resolved from other peaks in the energy spectra. Maximum Al-beam currents were near or above 10 μA with currents remaining above 5 μA even after an hour of sputtering. All the samples were mixed with niobium before loading into sample cathodes, but the combined sample GISP2/3/4 was measured after PRIME Laboratory switched to niobium as the binder for the AMS standards, which proved to be superior and cleaner in the AMS than the AMS standards used in the earlier measurements of the GISP2 samples that were mixed with silver. This might be one explanation for the considerably lower blank-level corresponding to the GISP2/3/4 measurement (Extended Data Table 3).

^{26}Al/^{27}Al background correction for the GISP2 samples. The corrections to the ^{26}Al/^{27}Al 'raw' ratios of our samples are less than 2% for the top sample GISP2/3/4 and 15% for the lower GISP5/6/7 sample (Extended Data Table 3). In addition to the traditional background correction by simply subtracting the mean ratio of the measured process blanks from the ^{26}Al/^{27}Al ratio of the samples, we chose to apply a time-progressive background correction that takes into account the different run times of the two samples and the blanks. This can be important, because our experience indicates that the most likely source of the ^{26}Al blank is ion source memory, rather than addition of ^{26}Al during chemical processing. The ^{26}Al machine memory derived from higher ratio samples, such as standards, previously measured in the ion source, is a function of measurement time, and thus samples measured for longer accumulate higher levels of memory ^{26}Al. We monitored the machine memory by measuring multiple blanks for periods of time comparable to the periods for which the corresponding samples were measured (Extended Data Table 3). The number of mass 26 counts in the blanks was converted into counts of ^{26}Al per minute of run time and this count rate was subtracted from the raw count rate of the samples measured at about the same time. The total error in the ratio based on this correction reflects the uncertainties of the sample measurement together with the uncertainties of this correction. We note that the two correction procedures applied here yield very similar results (Extended Data Table 3).

Data analysis. We describe how we infer information about the exposure history of GISP2 subglacial bedrock from the measured ^{26}Al and ^{10}Be concentrations. The three basic characteristics of these data are: (1) cosmogenic-nuclide concentrations decrease with depth in the core; (2) concentrations decrease less rapidly than we would expect if the bedrock surface in the core had been the land surface during exposure; and (3) the measured ^{26}Al/^{10}Be ratio in these samples is substantially less than the surface production ratio of 6.75. The change in nuclide concentration with depth in the core (as described in detail below) is diagnostic of the depth below the surface at which production took place. The ^{26}Al/^{10}Be ratio is important because these nuclides are produced at a fixed ratio during surface exposure (^{26}Al/^{10}Be = 6.75; ref. 22), but ^{26}Al has a shorter half-life (0.7 Myr; ref. 18) than ^{10}Be does (1.4 Myr; refs 16 and 17). A sample that has experienced a single period of surface exposure has a ^{26}Al/^{10}Be ratio that conforms to the production ratio, but if the sample is then buried sufficiently deeply to halt additional nuclide production, the ^{26}Al/^{10}Be ratio decreases over time with a half-life of 1.4 Myr.

It is not possible to invert our observations to yield a single unique exposure history because there exist an infinite number of exposure histories that are consistent with these observed characteristics. Thus, we here propose a number of broad classes of exposure histories and ask if they can be fitted to the observations. For example, if we propose that the observations can be explained by a single period of surface exposure followed by a single period of ice cover, we can ask whether there exist any values for the exposure and burial durations that provide an acceptable fit to the observations. If no such values exist, this class of exposure histories is not consistent with the observations. If such values do exist, they define exposure histories that are consistent with the observations and thus could potentially represent the true exposure history of the site.

We will use this reasoning to support three main conclusions. First, although the present bedrock surface in the core must have been covered by some additional rock, soil or ice during past periods of cosmic-ray exposure, the thickness of this material cannot have been more than a few metres. Thus, the observations require the absence of the GIS during periods of cosmic-ray exposure. Second, the longest possible length of time that the present ice sheet could have remained continuously present at the core site is approximately 1.1 Myr. Third, although there exist many scenarios of ice-sheet change that are consistent with the observations, all these scenarios require the absence of the ice sheet at the core site during some or all Pleistocene interglaciations.

We now discuss the depth-dependence of the cosmogenic-nuclide concentrations. Production of ^{10}Be and ^{26}Al occurs both by high-energy neutron spallation and by muon interactions. At and immediately below the surface, most production is by spallation, and spallogenic production rates decrease exponentially with depth with an e-folding length near 140 g cm^{-2} (this value is appropriate for high latitude). With increasing depth, spallogenic production becomes less important than production due to deeply penetrating muons, which has a longer e-folding length (>1,500 g cm^{-2}, increasing with depth[24]). A single exponential curve fit to our observed nuclide concentrations has an an e-folding length intermediate between these two (262 g cm^{-2}, although because a single exponential function does not fit the data adequately, this value is not physically meaningful). Thus, the observed nuclide concentrations reflect both spallogenic and muon production. In other words, the observations are not consistent with a single period of exposure during which the present bedrock surface was the land surface (in this case the measured concentrations would decrease with an e-folding length near 140 g cm^{-2}). The fact that we observe an apparent e-folding length that is longer than expected for spallogenic production alone requires that a large fraction of the measured nuclide concentrations is the result of production by muons, which means that production took place farther below the surface than the samples are now below the bedrock surface. The data are also not consistent with exposure more than a few metres below the surface (in which case the contribution from spallogenic production would be negligible, and the concentrations would decrease with an e-folding length characteristic of muon production).

Extended Data Fig. 1 shows that the depth dependence of the production rate immediately below the surface has a much shorter e-folding length than has the depth dependence of the measured nuclide concentrations. In other words, an exposure model including a period of surface exposure, with negligible erosion, during which time the bedrock surface was the land surface, does not fit the data. We also show the result of assuming that the bedrock surface was covered by additional mass during the period of exposure. In other words, we are trying to fit the measurements to the production profile by adjusting how far the bedrock

surface was below the actual land surface at the time that exposure took place. We represent this by an additional mass cover thickness covering the bedrock surface. The best-fitting cover thickness, the fit of which is shown in Fig. 2 and also in Extended Data Fig. 1, is 350 g cm^{-2}. A nominal (Monte Carlo) uncertainty on this value derived only from the measurement uncertainties is ±20 g cm^{-2}. However, the best-fitting cover thickness also depends on the assumed mean atmospheric pressure at the site during exposure (which, as discussed in more detail below, is not well constrained), because this affects the relative proportion of spallogenic and muon-induced production. For example, reducing the atmospheric pressure by 25 hPa (equivalent to an increase in site elevation of about 200 m) would imply a best-fitting cover thickness of 375 g cm^{-2} instead of 350 g cm^{-2}. By this argument, the nominal measurement uncertainty of 20 g cm^{-2} does not provide a physically meaningful error estimate.

350 g cm^{-2} of mass thickness is approximately 1.3 m of rock, 1.7 m of soil or 3.8 m of ice. Thus, the simplest explanation for the observed depth-dependence of the measured nuclide concentrations is that the bedrock surface was covered by 1–4 m of soil, sediment, rock or ice when exposure took place. Later, for completeness, we consider a more complicated and geologically less likely potential explanation involving a long period of continuous surface exposure at a relatively high erosion rate, and show that it does not provide as good a fit to the measurements. To summarize our discussion of the depth-dependence of the measured nuclide concentrations, (1) this shows that the present bedrock surface was probably covered by some additional shielding at the time of nuclide production, and (2) this requires that production took place within a few metres of Earth's surface. The observed nuclide inventory could not be the result of long residence under tens or hundreds of metres of ice; if it were, nuclide concentrations would decrease less with depth.

We now proceed by developing a forward model to compute the predicted nuclide concentrations in our samples given a specified exposure history. First, we describe our production-rate calculations in detail. We assume a reference ^{10}Be production rate due to spallation of 4.1 atoms g^{-1} yr^{-1}, which follows ref. 37 but is adjusted for the difference in muon interaction cross-sections between those used here and those used in that work; a ^{26}Al/^{10}Be production ratio of 6.75 (ref. 22); and the production rate scaling method of ref. 38, as implemented in ref. 37. We assume that the land surface at the core site during periods of exposure is located at sea level, and compute the atmospheric pressure using the spatially variable atmosphere of ref. 37. We note that this is speculative because both the elevation of the site and the atmospheric pressure distribution would most probably be very different in the absence of the GIS; in addition, both would experience transient changes during ice-free periods. We take the ^{10}Be decay constant to be 4.99×10^{-7} (refs 16 and 17) and the ^{26}Al decay constant to be 9.83×10^{-7} (ref. 39). We compute production rates due to muons using the MATLAB implementation in ref. 37 of the method of refs 20 and 21. However, we use muon interaction cross-sections derived from fitting this method to measurements from a deep sandstone core in Antarctica. These measurements are reported in ref. 40; the fitted cross-sections are: for ^{10}Be, $f^* = 0.0011$ and $\sigma_0 = 0.81$ μb; for ^{26}Al, $f^* = 0.0084$ and $\sigma_0 = 13.6$ μb (these symbols correspond to those used by refs 20 and 21). These differ from the values given in ref. 41, because we are using different code to compute the muon fluxes. Note that our main conclusions in this paper relate to the duration of ice cover of the site, which is sensitive to the values we use for the ^{10}Be and ^{26}Al decay constants and the ^{26}Al/^{10}Be production ratio, but is insensitive to inaccuracies in the absolute magnitude of the production rates. This is important because the uncertainty in our knowledge of the elevation and atmospheric pressure prevailing at the site during ice-free periods means that we are unlikely to be accurately estimating surface production rates when past exposure took place.

We now describe the model calculation of the nuclide concentrations expected for a particular exposure history. Assuming an exposure history is equivalent to specifying the mass cover thickness z_c (mass thickness has units of grams per square centimetre) above the surface of the bedrock in the core at all past time. We define a time coordinate t that is zero at the present time and positive for past times, and then define an exposure history as a function $z_c(t)$ that describes the variation in z_c over time. For example, if the exposure history consists of one period of surface exposure followed by one period of cover by the full thickness of the Greenland ice sheet, then $z_c(t)$ equals zero during the period of exposure and is effectively infinite (ice thickness of the order of 100 m or greater is effectively infinite burial, that is, zero cosmogenic-nuclide production) during the period of ice cover. Another example is that surface erosion during ice-free periods would be represented by $z_c(t)$ steadily decreasing during the ice-free period at the rate of erosion.

Given an exposure history $z_c(t)$ and also knowing the production rate of nuclide k as a function of mass depth z, $P_k(z)$ (atoms g^{-1} yr^{-1}; calculated as described above), the predicted average concentration $N_{j,k}$ (atoms g^{-1}) of nuclide k in sample j at the present time is given by the integral:

$$N_{j,k} = (z_{j,\mathrm{bottom}} - z_{j,\mathrm{top}})^{-1} \int_{z_{j,\mathrm{top}}}^{z_{j,\mathrm{bottom}}} \int_{0}^{t_{\max}} P_k(\zeta + z_c(\tau)) \exp(-\lambda_k \tau) \mathrm{d}\tau \mathrm{d}\zeta \qquad (1)$$

where $z_{j,\mathrm{bottom}}$ and $z_{j,\mathrm{top}}$ are the top and bottom mass depths (in units of g cm^{-2}) of sample j below the bedrock surface, $z_c(t)$ is the exposure history—that is, the mass thickness (in g cm^{-2}) covering the bedrock surface as a function of time t (in years)—λ_k is the decay constant (in yr^{-1}) of nuclide k, and τ and ζ are variables of integration. As noted above, the time coordinate is defined to be zero at the present time and positive for past times: $t_{\max}$ is the time that the exposure history begins, and the nuclide concentration at $t_{\max}$ is zero. In the case that the sample is composed of multiple core segments, we evaluate the integral for each segment separately and then use the weight of quartz contributed by each core segment to calculate the average nuclide concentration in the combined sample. We evaluate this integral using the default numerical integration routine in MATLAB software with, for computational efficiency, a piecewise-linear approximation of $P_k(z)$ defined on a logarithmic grid.

The misfit statistic we use in comparing predicted to measured nuclide concentrations is the chi-squared statistic χ^2 using the measurement uncertainty in the nuclide concentrations as the weighting. We note that because the measurement uncertainties for ^{10}Be are much smaller than those for ^{26}Al, this statistic assigns greater importance to the ^{10}Be measurements and is more sensitive to whether the model matches the depth profile of ^{10}Be concentrations than to whether the model matches ^{26}Al/^{10}Be ratios. A fitting statistic that weighted the ^{26}Al data set equally with the ^{10}Be data set might yield slightly different conclusions, although we tested this and did not find a large effect on the main conclusions of the paper. Another important point about the fit statistic is that we assume that the measured core depths and density are exact. This is unlikely to be strictly true, because the core is jointed and somewhat fragmented, with short missing sections (Fig. 1), and small vertical displacements of the core segments during recovery are likely. Thus, the probabilities of fit to the observations discussed below are likely to underestimate the model performance; if we accounted for additional uncertainties in depth and density we would obtain higher probabilities of fit.

We begin by fitting the simplest possible exposure history that can explain our data to the measurements. Several observations lead us to this simplest possible exposure history; by 'simplest', we mean the exposure history that has the fewest distinct periods of surface exposure or burial by the ice sheet. First, the fact that we observe substantial cosmogenic-nuclide concentrations that decrease with depth indicates that a period of surface exposure occurred. Second, the depth-dependence of the concentrations, as discussed above, indicates that the bedrock surface was probably shielded by additional cover at the time that exposure took place. Third, the fact that the observed ^{26}Al/^{10}Be ratio is lower than the surface production ratio indicates that the samples have been shielded from the surface cosmic-ray flux, presumably by the present GIS, for some time (Extended Data Table 1). These three observations show that the simplest possible exposure model that can explain our observations must include at least one period of surface exposure, at least one period of burial, and some thickness of additional cover of the bedrock surface. For the time being we assume zero surface erosion at all times. We refer to this model henceforth as 'model 1'.

Extended Data Fig. 2 shows the results of fitting model 1 with three adjustable parameters (the duration of a single period of exposure, the duration of a subsequent period of burial, and the cover thickness above the present bedrock surface) to the observations. Model 1 fits the observations with reduced χ^2 of 1.9 for 4 degrees of freedom, which is a probability of fit of 0.11. Given that the probability-of-fit is probably biased low as discussed above, we view this as an acceptable fit. As discussed above, note that the fitting statistics here are disproportionately affected by whether or not the depth profile fits the relatively high-precision ^{10}Be measurements; because the model is overparameterized in relation to a single ^{26}Al/^{10}Be pair, the exposure time and burial time parameters could be chosen to fit either pair exactly. The best-fitting exposure history here has 280 kyr of exposure under 350 g cm^{-2} of additional cover, followed by 1.1 Myr of burial. A Monte Carlo uncertainty analysis considering only measurement uncertainties indicates formal uncertainties in these parameters as follows: exposure time 282 ± 31 kyr; burial time 1.110 ± 0.092 Myr. If we include uncertainties in decay constants, the uncertainty on the burial time is 0.109 Myr. We note that these uncertainties only apply if model 1 is assumed to be correct a priori. In reality, of course, although model 1 is consistent with the cosmogenic-nuclide measurements taken by themselves, geological and palaeoclimate considerations show that it is unlikely. In addition, the best-fitting exposure duration

for this model is also somewhat dependent on the assumed atmospheric pressure. For example, decreasing the assumed atmospheric pressure by 25 hPa (as we did above in the discussion of cover thickness, which is approximately equivalent to a 200-m increase in elevation) decreases the best-fitting exposure duration by 6 kyr (to 276 kyr). However, this does not affect the estimate of burial duration.

Fitting model 1 highlights the fact that because of the additional cover thickness that we need to match the measured attenuation length of the ^{10}Be concentration depth profile, the exposure time to account for the observed nuclide concentrations must be on the order of 10^5 years. Taken out of this depth profile context, the measured nuclide concentrations are similar to typical surface concentrations in modern deglaciated landscapes that have experienced Holocene surface exposure only of the order of 10,000 years. However, because exposure took place below the land surface (below 1.3 m of rock, 1.7 m of soil or 3.4 m of ice; see above), they actually record an exposure history that is much longer than a single interglacial, or even a few interglacials.

For completeness, we now consider another theoretical explanation for the fact that the depth-dependence of the measured concentrations is inconsistent with spallogenic production alone. This could occur if the bedrock surface had been allowed to erode at a steady rate while continuously exposed at the surface for a long period of time. A long period of steady erosion means that a large fraction of the near-surface nuclide inventory was actually produced at depth by muons, and has been brought to the surface by erosion. This results in a longer apparent attenuation length near the surface than would be expected for spallogenic production only. In effect, steady erosion acts to drag the lower, longer-attenuation-length, part of the profile towards the surface. This scenario is unlikely for geological and palaeoclimatic reasons because it takes a long period of steady erosion for the muon-produced inventory to reach steady state. For example, at an erosion rate of 30 m Myr^{-1} (see below) it would take of the order of 1 Myr of continuous exposure and steady erosion for the muon-produced ^{10}Be inventory to reach steady state. In other words, although the steady-state scenario removes the need for additional sediment cover of the bedrock surface, it requires a very long period of undisturbed exposure before burial.

To evaluate this possibility, we fitted a model ('model 1B') with the following exposure history. First, the bedrock surface is the land surface—there is no sediment cover—and it erodes at a steady rate for long enough that nuclide concentrations reach a steady state in which production is balanced by nuclide loss via surface erosion and radioactive decay. Second, it is buried under ice for a period of time. Model 1B has two free parameters: the steady erosion rate and the burial duration. The best fit of model 1B to the data (Extended Data Fig. 2) has steady erosion at 32 m Myr^{-1} followed by 1.06 Myr of burial. This does not fit the data as well as model 1; the reduced χ^2 is 5.85 for 5 degrees of freedom, implying a probability-of-fit <0.0001. Model 1B has difficulty matching both the depth dependence of the ^{10}Be concentrations and also the ^{26}Al/^{10}Be ratio. Perhaps more importantly, as discussed above, this scenario requires more than about 1 Myr of undisturbed steady erosion before burial, which is geologically unlikely in the light of evidence for glaciation of Greenland during the Pleistocene. In addition, the observation of high concentrations of meteoric ^{10}Be in sediment in GISP2 basal ice[4] would be inconsistent with an erosion rate as high as 30 m Myr^{-1}. If the sediment analysed by ref. 4 has been buried under ice since 1.1 Myr ago as our ^{26}Al/^{10}Be ratios indicate, then a steady-state balance calculation based on Figure 3B of ref. 4 would suggest an erosion rate of 7 m Myr^{-1}, which would be typical of early Pleistocene cratonic landscapes in North America[42]. If the erosion rate were 7 m Myr^{-1}, we could not match the observed ^{10}Be depth profile with a steady-erosion model unless we also allowed for sediment cover of the bedrock surface. Thus, we conclude that model 1B is unrealistic and the most likely explanation for the observed depth-dependence of the ^{10}Be and ^{26}Al concentrations is that the present bedrock surface was covered by around 1–4 m of additional cover at the time that exposure took place.

To complete the discussion of two-stage exposure models, we observe that although we have considered two-stage models with no erosion and sediment cover (model 1) and steady-state erosion with no sediment cover (model 1B, which we have subsequently rejected), there exist intermediate scenarios that provide an acceptable fit to the data. Here we perform a Monte Carlo simulation in which we consider only two-stage exposure histories with a single period of exposure followed by a single period of burial, but allow the exposure duration, burial duration, erosion rate during exposure, and cover thickness to float. This model ('model 1C') is effectively overparameterized and finds many combinations of the parameters that fit the data acceptably well. Here we define 'acceptable' to be reduced $\chi^2 = 2.6$ for 3 degrees of freedom; that is, we cannot reject the model at 95% confidence. Extended Data Fig. 3 shows that a wide variety of combinations of exposure time, burial time and cover of the bedrock surface will adequately fit the observations. This exercise also demonstrates that the best-fitting burial duration is only very weakly sensitive to the trade-off between exposure time, erosion rate and cover thickness. No matter what the exposure time, cover thickness and erosion rate before burial, the observed ^{26}Al/^{10}Be ratio constrains the burial time for any two-stage exposure history to be close to 1.1 Myr.

Finally, we now turn to exposure models with more than two stages. As has been discussed at length in the literature in the context of ^{26}Al–^{10}Be concentrations observed in bedrock that has been covered by ice in the past (for example, see ref. 43), there are an infinite number of possible exposure-burial histories that will yield our observed ^{26}Al and ^{10}Be concentrations and ratio. In this case, however, all possible exposure histories share the constraint that at least one period of exposure must have ended no earlier than 1.1 ($\pm$0.1) Myr ago. If this were not the case—if the present ice sheet at the core site had been in place for more than 1.1 Myr—the ^{26}Al/^{10}Be ratio in these samples would be lower than we observe at present. For example ref. 4 hypothesized that the GISP2 site has been continuously covered by the GIS since 2.7 Myr ago. If this hypothesis were correct (and if we also assume 350 g cm^{-2} of cover of the bedrock surface as discussed above, although this is not a critical assumption), the observed ^{26}Al/^{10}Be concentration in our samples could be no higher than 2.

In this section, therefore, we propose a series of representative multi-stage exposure–burial scenarios and determine whether or not they are consistent with the observations. We also use the observation from fitting model 1C (Extended Data Fig. 3) that the burial duration is not sensitive to the particular combination of erosion rate and cover of the bedrock surface during exposure periods, to limit the parameter space somewhat. Henceforth we will assume that the bedrock surface is covered by 350 g cm^{-2} of cover during exposure periods, and the surface erosion rate is zero. If this were not correct, that is, if the erosion rate were greater than zero during exposure periods, this assumption would lead us to underestimate the duration of exposure periods slightly. If we can take the meteoric ^{10}Be measurements of ref. 4 as a guide to the likely erosion rate as discussed above, this effect is not important to any of our conclusions. Note that the relevance of underestimating the erosion rate on the inferred duration of exposure periods can be estimated from Extended Data Fig. 3.

The first many-stage exposure history we consider is an endmember, opposite from the simplest possible exposure history of model 1, in which the site has been cyclically covered and uncovered by ice for long enough that nuclide concentrations have reached a dynamic steady state, in which nuclide production during interglacial periods when the site is exposed is equal to radioactive decay of the existing nuclide inventory during each cycle (henceforth 'model 2'). We assume 350 g cm^{-2} cover and zero erosion as discussed above, and we assume 100-kyr durations for glacial–interglacial cycles, so model 2 has one free parameter: the length of time during each cycle that the site is ice-free. Palaeoclimate data, of course, indicate that 100-kyr glacial–interglacial periodicity was not evident before about 0.8 Myr ago, so model 2 is only an approximate representation of palaeoclimate data. Instead, it represents a simple, but infinitely long, exposure history as a contrast to the shortest possible exposure history that can explain the data (model 1). Interestingly, even though model 2 has only one fitting parameter (the fraction of each 100-kyr cycle during which the site is ice-free) we can obtain a good fit to the measurements (Extended Data Fig. 4). The best-fitting interglacial duration is 8,000 years, which fits the data with reduced $\chi^2 = 1.75$ for 6 degrees of freedom, that is, a probability-of-fit of 0.11, which is indistinguishable from the probability of fit for model 1.

We have now discussed two endmember models that fit the data: a single period of middle Pleistocene exposure followed by 1.1 Myr of continuous burial (model 1; this is the shortest possible exposure model that can fit the data), and a dynamic steady state model in which the GIS is absent for 8 kyr of each 100-kyr-long glacial–interglacial cycle (Model 2; as this model is infinitely long, it is the longest possible exposure model that can fit the data, although it is not uniquely so). There are many intermediate models that also fit the data. These are constrained by the general principle that if we start with model 1 and add any periods of exposure during the most recent 1.1 Myr, then we must also add periods of burial before 1.1 Myr ago to maintain the observed ^{26}Al/^{10}Be ratio. We show several such models, one of which is shown in Fig. 3 as model 3 (see also Extended Data Fig. 4). All these models have the same probability of fit, which is also the same as for model 1 above (and, in fact, they predict exactly the same ^{26}Al and ^{10}Be concentrations).

To summarize, we present endmember exposure models and a wide variety of exposure models between those endmembers that can explain the observed ^{10}Be and ^{26}Al concentrations in the GISP2 bedrock core. The important point of these calculations is not that any one of these scenarios is either uniquely most likely or most favoured by other palaeoclimate data, but that exposure histories that include ice-free conditions during any or all Pleistocene interglaciations (before the present one) can be fitted to the data. However, a scenario in which the present ice sheet has existed continuously for more than the last 1.1 Myr does not fit the observations under any circumstances.

Code availability. MATLAB code used to perform all data analysis in this paper is available at http://hess.ess.washington.edu/repository/GISP2.

Erosion of bedrock under the GIS summit. First, the observation by Bierman and others[4] of high concentrations of meteoric ^{10}Be in soil within GISP2 basal ice is not consistent with any substantial erosion of the underlying bedrock. Second, available data indicate that erosion from normal ice-sheet processes is very slow, and inadequate to remove a substantial amount of bedrock underneath the GIS summit. Summarized by ref. 25, the basal $h_s \approx 13$ m of ice in the GISP2 ice core contained a volume-concentration of silt $c_s \approx 0.001$. Measured borehole deformation indicates a mean horizontal flow velocity for this silty ice of $u \approx 0.07$ m yr^{-1}. If the rock material is sourced uniformly from the $L \approx 2.8 \times 10^4$ m flow line extending through GISP2 from the ice divide at GRIP, then the steady-state erosion rate is $E = h_s c_s u/L \approx 3 \times 10^{-8}$ m yr^{-1} of rock, or 3 cm per million years[25].

Basal silty ice chronologies and bedrock exposure ages. The new results of Yau *et al.*[10] on the antiquity of basal ice from the Dye-3 (southern Greenland) and GRIP (summit) ice cores might at first seem to raise questions about the results presented here, but may indeed provide a consistent history and point to ways to constrain that history more tightly. Using the measured ratios of argon isotopes in air trapped in the basal ice of the cores, together with the rise in atmospheric ^{40}Ar over time linked to radioactive decay of ^{40}K in rocks and subsequent degassing, the oldest ages of replicates of air that Yau *et al.*[10] found in ice at the base of the GRIP core gave 970 ± 140 kyr (and 400 ± 170 kyr in the Dye-3 core); much younger air was also present. In the light of the possibility of contamination by local radiogenic production, the ice containing the oldest air could be even older.

These findings are not themselves inconsistent with our data, because our main conclusion is prolonged periods of nearly ice-free Greenland during the Pleistocene, and the simplest GIS scenario consistent with our data that also gives an upper bound for the maximum period the GIS was continuously present (the maximum-stability scenario '1' in Fig. 3) is that of approximately 280 kyr of ice-free Greenland summit before 1.1 Myr ago followed by burial by the GIS since then. Alternatively, it could be that the old basal ice at GRIP and Dye-3 was preserved during periods of nearly vanished GIS in the eastern or northeastern Greenland highlands and subsequently flowed to their current positions. Modelling of the GIS under warming, or under cooling from warmer conditions, often produces a greatly reduced ice volume together with ice-free conditions across most of the island including at or near GISP2, but an intact small ice cap on the highlands to the east (for example, see ref. 27); the simulated position of the western boundary of that ice cap relative to GISP2 and GRIP (which is 28 km east of GISP2) depends on the model, including its resolution, and on the forcing, history, and so on (Fig. 1). The broad picture of retreat to and advance from a greatly reduced eastern ice cap is fairly widespread across models, and histories can be simulated in which substantial ice-sheet shrinkage and regrowth occur with deglaciation of GISP2 and GRIP locations, or with deglaciation of GISP2 but not of GRIP. Notably, if advance occurs from an extant ice cap over adjacent surfaces, old ice will move over younger surfaces. Thus, our results plus those of Yau *et al.*[10] are consistent with the idea of preservation of old ice in the eastern highland areas during prominent interglacials, as discussed in the main text. The bedrock cosmogenic nuclides and the basal gas isotopes provide independent, potentially complementary constraints, and together might deliver a rather tight framework for ice sheet models.

Data availability. The data used in this study are available in Extended Data Tables 1–3.

31. Schaefer, J. M. *et al.* High frequency Holocene glacier fluctuations in New Zealand differ from the northern signature. *Science* **324,** 622–625 (2009).
32. Davis, J. C. *et al.* LLNL/UC AMS Facility and Research-Program. *Nucl. Instrum. Methods Phys. Res. B* **52,** 269–272 (1990).
33. Granger, D. E. *et al.* New cosmogenic burial ages for Sterkfontein Member 2 Australopithecus and Member 5 Oldowan. *Nature* **522,** 85–88 (2015).
34. Paul, M. Separation of isobars with a gas-filled magnet. *Nucl. Instrum. Methods Phys. Res. B* **52,** 315–321 (1990).
35. Timmers, H., Weijers, T. D. M. & Elliman, R. G. Unique capabilities of heavy ion elastic recoil detection with gas ionization detectors. *Nucl. Instrum. Methods Phys. Res. B* **190,** 393–396 (2002).
36. Fifield, L. K., Tims, S. G., Gladkis, L. G. & Morton, C. R. ^{26}Al measurements with ^{10}Be counting statistics. *Nucl. Instrum. Methods Phys. Res. B* **259,** 178–183 (2007).
37. Balco, G., Stone, J. O., Lifton, N. A. & Dunai, T. J. A complete and easily accessible means of calculating surface exposure ages or erosion rates from Be-10 and Al-26 measurements. *Quat. Geochronol.* **3,** 174–195 (2008).
38. Stone, J. Air pressure and cosmogenic isotope production. *J. Geophys. Res.* **105,** 23753–23759 (2000).
39. Nishiizumi, K. Preparation of Al-26 AMS standards. *Nucl. Instrum. Methods Phys. Res. B* **223/224,** 388–392 (2004).
40. Borchers, B. *et al.* Geological calibration of spallation production rates in the CRONUS-Earth project. *Quat. Geochronol.* **31,** 188–198 (2016).
41. Phillips, F. M. *et al.* The CRONUS-Earth project: a synthesis. *Quat. Geochronol.* **31,** 119–154 (2016).
42. Rovey, C. W. & Balco, G. Paleoclimatic interpretations of buried paleosols within the pre-Illinoian till sequence in northern Missouri, USA. *Palaeogeogr. Palaeoclimatol. Palaeoecol.* **417,** 44–56 (2015).
43. Bierman, P. R., Marsella, K. A., Patterson, C., Davis, P. T. & Caffee, M. Mid-Pleistocene cosmogenic minimum-age limits for pre-Wisconsinan glacial surfaces in southwestern Minnesota and southern Baffin island: a multiple nuclide approach. *Geomorphology* **27,** 25–39 (1999).

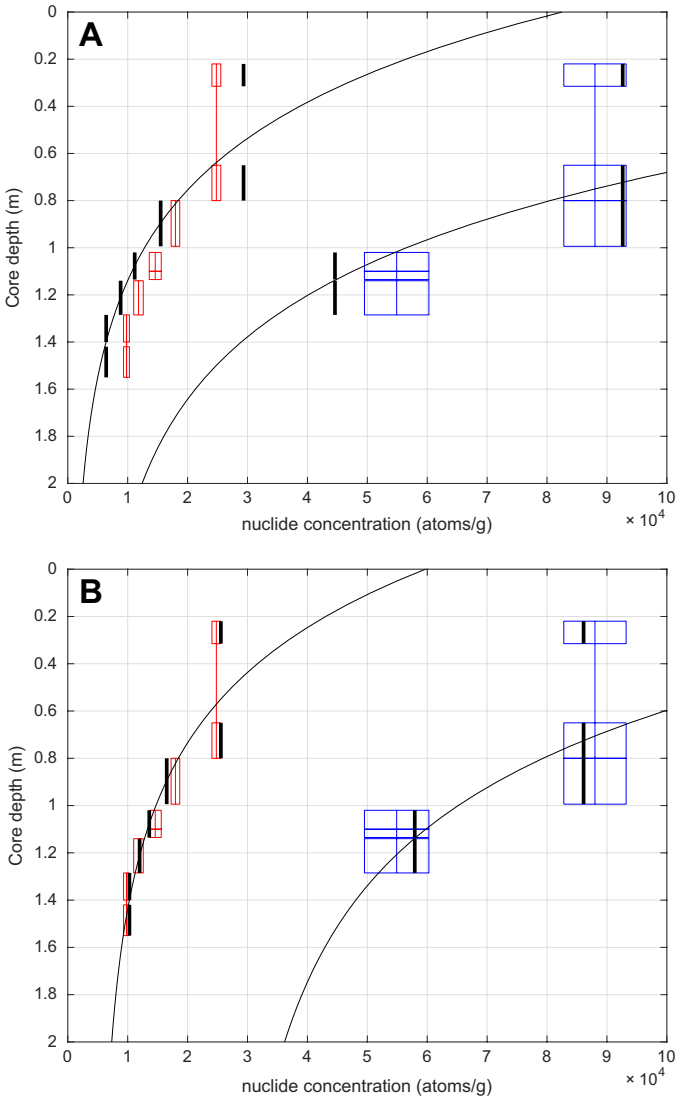

Extended Data Figure 1 | ^{10}Be and ^{26}Al concentrations compared to production rates. ^{10}Be ($n = 5$) and ^{26}Al ($n = 2$) concentration–depth profiles compared to the depth dependence of nuclide production rates (including both spallogenic and muon production). In both **a** and **b**, the red and blue boxes represent ^{10}Be (red) and ^{26}Al (blue) measurements. The vertical dimension of each box represents a distinct segment of core, and vertical lines connect multiple core segments that were amalgamated for each ^{10}Be or ^{26}Al analysis. In most cases amalgamated segments were adjacent to each other, but in some cases (for example, the uppermost two core segments), they were separated by gaps. The width of the boxes shows measurement uncertainty (1σ; see Extended Data Table 1) on nuclide concentrations. In **a**, we attempt to fit the observations by assuming that the bedrock surface is the land surface, the erosion rate is zero, and by allowing the duration of a single period of exposure to vary. For this exercise we treat ^{10}Be and ^{26}Al separately, that is, the predictions are not forced to obey the production ratio. The continuous thin black lines show predicted nuclide concentrations for this model, and the discontinuous, darker, black bars show predicted nuclide concentrations averaged over depth ranges corresponding to each analysis. The black bars, therefore, are the model predictions that we compare to the measurements. This model cannot be fitted to the data, because observed nuclide concentrations do not decrease as rapidly as they would if the bedrock surface were the land surface during exposure. In **b**, we perform the same fitting exercise, but also include a thickness of shielding mass above the bedrock surface as an additional fitting parameter. This removes the systematic misfit shown in **a** and makes it possible to fit the observations. A cover thickness of 350 g cm^{-2} best fits the observations.

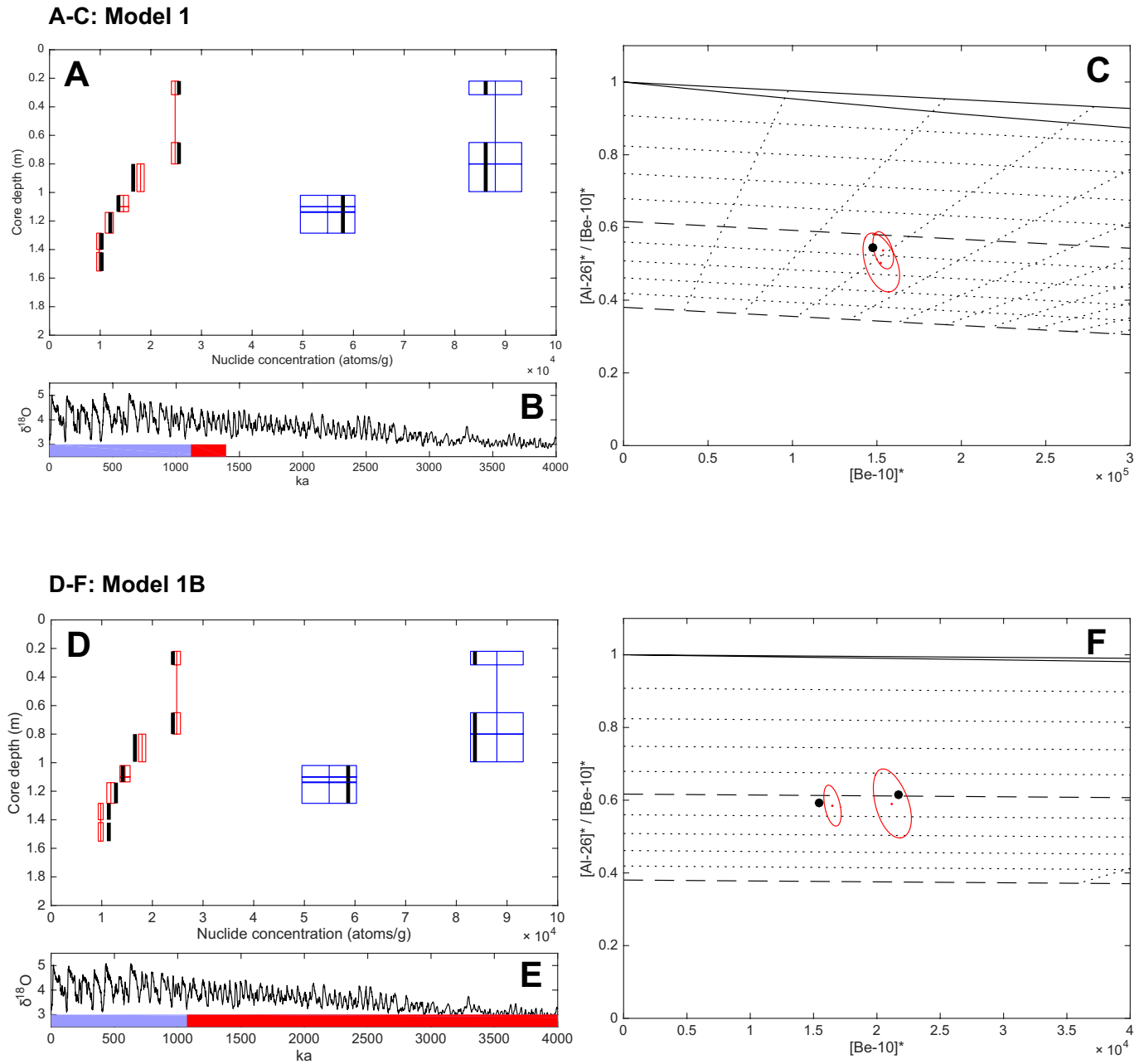

Extended Data Figure 2 | Two-stage exposure histories fit to ^{10}Be and ^{26}Al measurements. In **a** and **d**, the red and blue boxes represent ^{10}Be (n = 5; red) and ^{26}Al ($n = 2$; blue) measurements. The vertical dimension of each box represents a distinct segment of core, and vertical lines connect multiple core segments that were amalgamated for each ^{10}Be or ^{26}Al analysis. In most cases amalgamated segments were adjacent to each other, but in some cases (for example, the uppermost two core segments), they were separated by gaps. The width of the boxes shows measurement uncertainty (1σ; see Extended Data Tables 2 and 3) on nuclide concentrations. The thick black lines are nuclide concentrations predicted for each core segment by the best-fitting parameters of each model. **b** and **e** show the exposure history implied by the best-fitting parameters of each model compared to the LR04 oxygen isotope stack from ref. 30. Red bars represent periods of surface exposure and blue bars periods of cover by the ice sheet. **c** and **f** show observed nuclide concentrations compared to model predictions for samples in which both ^{10}Be and ^{26}Al were measured, normalized to production rates at their respective depths implied by each model, on a two-nuclide diagram[29]. Red ellipses are 68% confidence regions for the nuclide concentrations including measurement uncertainties only, and black dots are nuclide concentrations predicted by best-fitting model parameters. The solid black lines show the simple exposure region; darker dashed lines are isolines of burial in increments of 1 Myr, and lighter dotted lines are isolines of exposure time in increments of 0.1 Myr. **a**, **b** and **c** show the fit of model 1, the simplest possible model that fits the data, which includes a single period of surface exposure, a single period of burial, 350 g cm^{-2} of cover thickness above the bedrock surface during exposure, and zero surface erosion. In **c**, nuclide concentrations are normalized to production rates at sample depths below this additional cover thickness. This model provides a good fit to the measurements. The exposure history implied by the best-fitting parameters for model 1 (280-kyr exposure, 1.1 Myr burial) provides a maximum limiting constraint on the length of time the present ice sheet has been continuously present at the core site. **d**, **e** and **f** show the fit of model 1B, which includes a long period of continuous exposure with steady surface erosion, a single period of burial, and zero additional cover thickness above the bedrock surface. In **f**, nuclide concentrations are normalized to production rates at sample depths below the bedrock surface. This model cannot be adequately fitted to the observations.

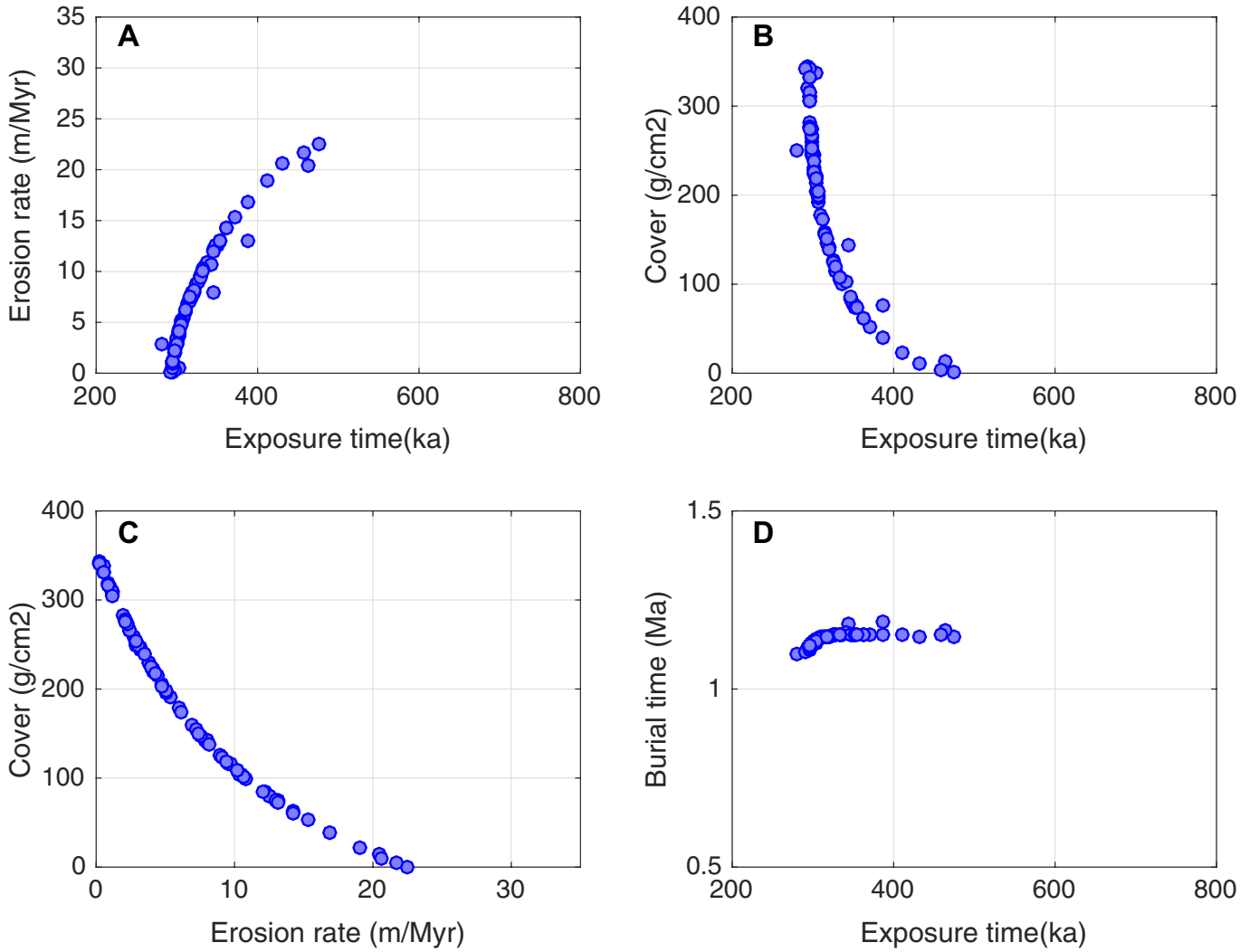

Extended Data Figure 3 | Two-stage exposure-burial models with four free parameters. a–d show parameter values for two-stage exposure-burial models with four free parameters (model 1C: free parameters are exposure time t_{exp}, burial time, surface erosion rate during exposure, and additional cover thickness above the bedrock surface during exposure periods) that yield acceptable fits to the observations. All panels show the same set of results; only the axes differ. Note that model 1 with best-fitting parameters (280-kyr exposure, 1.1 Myr burial, zero surface erosion, 350 g cm^{-2} cover thickness) is an endmember of this distribution.

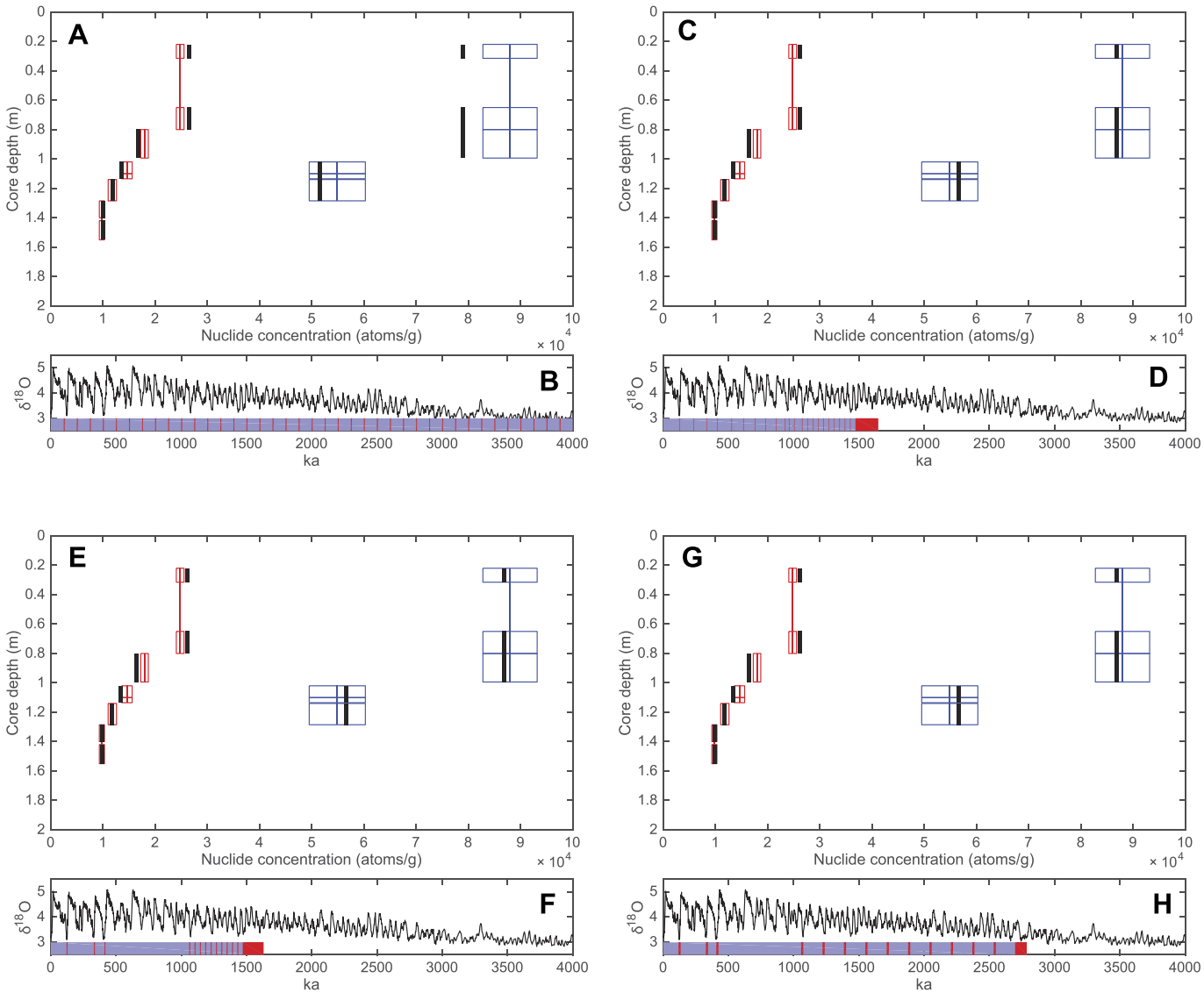

Extended Data Figure 4 | Many-stage exposure histories fitted to ^{10}Be and ^{26}Al measurements. In **a**, **c**, **e** and **f**, the red and blue boxes represent ^{10}Be (red) and ^{26}Al (blue) measurements. The vertical dimension of each box represents a distinct segment of core, and vertical lines connect multiple core segments that were amalgamated for each ^{10}Be or ^{26}Al analysis. In most cases amalgamated segments were adjacent to each other, but in some cases (for example, the uppermost two core segments), they were separated by gaps. The width of the boxes shows measurement uncertainty (1σ; see Extended Data Tables 2 and 3) on nuclide concentrations. The thick black lines are nuclide concentrations predicted for each core segment by the best-fitting parameters of each model. **b**, **d**, **f** and **h** show the exposure history implied by the best-fitting parameters of each model compared to the LR04 oxygen isotope stack from ref. 30. Red bars represent periods of surface exposure and blue bars periods of cover by the ice sheet. **a** and **b** show model 2, which is a dynamic steady state model with 100-kyr cycles. This model has one free parameter, which is the fraction of each cycle during which the site is ice-free, and assumes zero surface erosion and 350 g cm^{-2} cover thickness above the bedrock surface. The best-fitting length of ice-free periods for this model is 8,000 years. All other panels show models with ice-free conditions during some or all middle and late Pleistocene interglaciations, and have two free parameters: the duration of ice-free conditions during interglaciations, and the length of an initial ice-free period in the middle or early Pleistocene. **c** and **d** show a model in which the core site is ice-free during all interglacials within the period of 100-kyr-long glacial–interglacial cycles after 1.1 Myr ago, during an (arbitrarily long) series of short interglacials during 41-kyr-long glacial–interglacial cycles before 1.1 Myr ago, and during an initial longer period of exposure in the middle Pleistocene. The best-fitting duration of ice-free conditions during interglacials for this model is 4,200 years. **e** and **f** show ice-free conditions during MIS 9, MIS 11 and MIS 13, an (arbitrarily long) period of short ice-free interglaciations during 41-kyr-long cycles before 1.1 Myr ago, and an initial period of continuous exposure in the middle Pleistocene. The best-fitting duration of ice-free conditions during interglacials for this model is 7,400 years. **g** and **h** show ice-free conditions during MIS 9, MIS 11 and MIS 13, with (arbitrarily located) occasional ice-free periods in the early and middle Pleistocene. The best-fitting duration of ice-free conditions during interglacials for this model is 18,200 years.

Extended Data Table 1 | ^{10}Be and ^{26}Al concentrations of the GISP2 bedrock core

	Depth Top (m)	Depth Bottom (m)	mid-inventory depth (m)	Quartz (g)	^{10}Be (at/g)	1 sigma	^{26}Al (at/g)	1sigma	^{26}Al/^{10}Be	1 sigma	% error
GISP 2/3	0.22	0.65	0.44	12.66	24,800	740					
GAP	0.32	0.65									
GISP 4	0.80	1.00	0.89	17.88	18,000	720					
GISP 2/3/4	**0.22**	**1.00**	**0.49**	**30.54**	**20,800**	**520**	**88,000**	**5,200**	**4.23**	**0.27**	**6.4%**
GAP	1.00	1.02									
GISP 5/6	1.02	1.14	1.07	9.34	14,600	1,000					
GISP 7	1.14	1.29	1.21	8.81	11,800	800					
GISP 5/6/7	**1.02**	**1.29**	**1.14**	**18.15**	**13,300**	**1,300**	**55,000**	**5,400**	**4.14**	**0.57**	**13.9%**
GISP 8/9	1.29	1.55	1.40	8.87	9,800	490					

^{10}Be ($n = 5$) and ^{26}Al ($n = 2$) depth profile data from the GISP-2 core. The mid-inventory depth is the depth dividing each core piece into two halves of equal ^{10}Be and ^{26}Al inventory. See also core stratigraphy in Fig. 1. We measured 5 core samples for ^{10}Be. We combined the Al fractions (and splits for ^{27}Al analysis) of GISP2/3 and GISP4 as well as of GISP5/6 and GISP7 to get two precise ^{26}Al/^{27}Al measurements. The given 1σ errors reflect analytical uncertainties. To compare ^{10}Be and ^{26}Al measurements directly in the same sample and to calculate the ^{26}Al/^{10}Be ratio, we also show the ^{10}Be for GISP2/3/4 and GISP5/6/7, which are simply the sums of the measured ^{10}Be atoms in the respective ^{10}Be samples (GISP2/3 + GISP4 and GISP5/6 + GISP7). The 'Quartz' column gives the sample size.

Extended Data Table 2 | GISP2 bedrock ^{10}Be data

^{10}Be

Sample	Quartz (g)	^{9}Be carrier (mg)	^{10}Be/^{9}Be (10^{-15})	1 σ (10^{-15})	Uncertainty %	^{10}Be atoms	1 σ error	^{10}Be (atoms/g)	1 σ error	Max ^{10}Be Current (microAmps)
BLK1-2015Jul22			0.32	0.12	38%	3900	150			23
BLK2-2015Jul22			0.45	0.12	27%	5500	150			19
BLK3-2015Jul22			0.43	0.11	26%	5300	140			18
BLK4-2015Jul22			0.13	0.17	131%	1600	2100			20
BLK5-2015Jul22			0.39	0.12	31%	6000	190			17
GISP 2/3	**12.66**	**0.1889**	**25.20**	**0.82**	**3%**	**318,200**	**9,600**			21
GISP 2/3 corrected	**12.66**		**24.86**	**0.83**	**3%**	**313,500**	**9,405**	**24,760**	**740**	
GISP 4	**17.88**	**0.1894**	**25.72**	**0.96**	**4%**	**325,700**	**13,000**			18
GISP 4 corrected	**17.88**		**25.38**	**0.97**	**4%**	**321,300**	**12,852**	**17,970**	**720**	
GISP 2/3/4	**30.54**					**634,800**	**15,926**	**20,790**	**520**	
CB_2015May			0.05	0.10	200%	600	1200			26
BLK1-2015Apr17			0.38	0.09	24%	4700	1100			23
BLK2-2015Apr17			0.58	0.24	41%	7100	2900			20
BLK3-2015Apr17			0.01	0.22	2200%	100	2200			21
BLK4-2015Apr17			0.33	0.09	27%	4100	1100			21
BLK1-2015Apr21			0.3	0.09	30%	4000	1200			30
GISP 5/6	**9.34**	**0.1888**	**11.10**	**0.65**	**6%**	**140,000**	**8,400**			25
GISP 5/6 corrected	**9.34**		**10.80**	**0.71**	**7%**	**136,300**	**9,500**	**14,600**	**1,020**	
GISP 7	**8.81**	**0.1886**	**8.57**	**0.46**	**5%**	**108,000**	**5,400**			25
GIPS 7 corrected	**8.81**		**8.26**	**0.54**	**7%**	**104,100**	**7,300**	**11,800**	**830**	
GISP 5/6/7	**18.15**					**240,400**	**11,981**	**13,245**	**660**	
CB1_2014Apr23			0.05	0.25	500%	600	3000			25
CB2_2014Apr23			0.05	0.12	240%	600	1400			23
Blk-4_2014Feb28			0.30	0.11	37%	4000	1500			16
Blk-5_2014Feb28			0.23	0.39	170%	2800	4800			14
Blk-6_2014Feb28			0.19	0.49	260%	2300	6000			15
GISP 8/9	**8.87**	**0.1449**	**9.21**	**0.49**	**5%**	**89,200**	**4,500**			17
GISP 8/9 corrected	**8.87**		**8.97**	**0.49**	**5%**	**86,900**	**4,400**	**9,800**	**490**	

Sample and measurement details for the ^{10}Be samples, given with 1σ analytical uncertainty. Underlined values are the measurements used for further discussion. 'BLK' denotes process blanks, that is, ^{9}Be carrier that underwent a chemical procedure identical to that of the respective samples. We processed 3–5 such process blanks for each sample to ensure robust monitoring of any contamination; the background correction was done by subtracting the mean of the ^{10}Be atoms for all BLKs from the total ^{10}Be atoms in the corresponding sample. 'CB' denotes carrier blanks, that is, ^{9}Be carrier that did not undergo the sample and process blank chemistry, but was precipitated, dried, loaded in cathodes and sent directly to the Center for Accelerator Mass Spectrometry at the Lawrence Livermore National Laboratory for ^{9}Be/^{10}Be analysis. The difference between 'CB' and 'BLK' ^{10}Be atoms allows us to estimate the ^{10}Be contamination during the sample processing in the laboratory, which is small for the samples discussed here. During the 23 years of storage at the National Ice Core Laboratory in Boulder (1,600 m), the potential production of ^{10}Be and ^{26}Al in the core is of the order of several hundred atoms and is thus negligible compared to the measured values.

Extended Data Table 3 | GISP2 bedrock ^{26}Al data

^{26}Al

Sample	Quartz (g)	total ^{27}Al (mg)	natural ^{27}Al (mg)	$^{26}Al/^{27}Al$ (10^{-15})	1 σ (10^{-15})	Uncertainty %	^{26}Al (atoms)	1 σ error	^{26}Al (atoms/g)	1 σ error	Max ^{27}Al Current (microAmps)	Min ^{27}Al Current (microAmps)	Total ^{26}Al counts	Measurement time (min)
BLK5-2015Jul22				0.48	0.48	99.0%					11	8	2	
BLK3/4-2015Jul22				0.55	0.52	95.8%					10	9	2	
BLK2-2015Jul22				0.21	0.30	144.1%					10	6	1	
GISP-2/3/4	30.54	1.9117	0.8872	64.12	3.70	5.8%					11	7	351	35
GISP-2/3/4 corrected[1]				63.69	3.70	5.8%								
GISP-2/3/4 corrected[2]				62.99	3.72	5.9%	2,687,976	158,744	88,015	5,198				
BLK 5/6/7-2015Apr17				2.55	0.71	27.9%					8	4	13	
BLK2-2015Apr17				5.50	1.95	35.5%					9	4		
GISP-5/6/7	18.15	1.0232	0.3648	28.13	2.48	8.8%					8	4	143	55
GISP-5/6/7 corrected[1]				24.10	3.24	13.4%								
GIPS-5/6/7 corrected[2]				24.49	2.40	9.8%	996,688	97,675	54,914	5,382				
BLK1-2015Mar14				*2.48*	*0.82*	33.3%					*12*	*2*	*13*	
BLK2-2015Mar14				1.69	*0.64*	37.7%					*11*	*1*	*11*	
GISP 8/9	*7.36*	*1.7503*		***8.39***	***0.91***	***10.9%***					*12*	*1*	*92*	*100*

Sample and measurement details for the ^{26}Al samples. 'BLK' denotes process blanks, that is, ^{27}Al carrier that underwent a chemical procedure identical to that of the respective samples. Natural ^{27}Al was determined from two independent splits taken from the fully digested quartz sample by ICP-OES analysis, calibrated with in-house, gravimetrically prepared ^{27}Al standards cross-checked with commercial standards.

[1]The mean of the corresponding BLK values was subtracted from the sample to give the corrected value.

[2]To better account for memory effects during the AMS measurements, we performed a time-progressive background correction: $^{26}Al/^{27}Al$ measurements at PRIME laboratory are done in one-minute cycles and we directly subtracted BLK counts (counts per minute) closest to the measurement cycle of the corresponding sample.

Both background corrections yield very similar results, and we use the data based on the time-progressive background correction. See Methods for additional details. GISP2/3/4 and corresponding BLKs were analysed with AMS standards at PRIME mixed with niobium, while the other samples were measured versus AMS standards mixed with silver. The ^{26}Al measurement of the lowest sample, GISP8/9, given in small italics, was an initial sensitivity test: we added ^{27}Al carrier to the Al fraction after the cation column separation, so that any aluminium loss during the geochemical processing would go undetected; also, the 'count-rate-based blank correction' for this measurement was substantial and the measured $^{26}Al/^{27}Al$ ratio fell into the 10^{-15} range, which is near the detection limit of the AMS analysis and thus challenging; taken together, the ^{26}Al measurement of GISP8/9 is less reliable and not directly comparable to those of GISP5/6/7 and GISP2/3/4, and we base our discussion on these two upper samples.